



Dynamic control of defocus, astigmatism, and tilt aberrations with a large area foveal liquid crystal lens

BÉGEL LOUIS AND GALSTIAN TIGRAN**Center for Optics, Photonics and Laser, Department of Physics, Engineering Physics and Optics, Université Laval, 2375 Rue de la Terrasse, Québec, Québec G1V 0A6, Canada***tigran.galstian@phy.ulaval.ca**Received 14 January 2024; revised 8 March 2024; accepted 9 March 2024; posted 11 March 2024; published 29 March 2024*

We have recently reported the dynamic adjustment of the focal length in an electrically tunable liquid crystal “foveal” lens, the center of which can be shifted over a large working area. In the present work, we show that this design allows also the independent generation of astigmatism with arbitrary axis and tilt of the light wavefront by simply changing the phase and the voltage differences between 4 control electrodes. Furthermore, we also demonstrate the capability of generating highly localized negative (defocusing) lenses with the same device by using a dual frequency liquid crystal. © 2024 Optica Publishing Group

<https://doi.org/10.1364/AO.517797>

1. INTRODUCTION

Liquid crystals (LCs) have been successfully used in pixelated optical devices, such as LC displays (LCDs) and spatial light modulators (SLMs); see, e.g., [1,2]. However, for many mobile applications, these devices are cumbersome and costly. Adaptive gradient index (GRIN) optical devices (such as tunable lenses; see, e.g., [3–7]) represent an interesting alternative for using LC materials in optical imaging or vision systems since, compared to LCDs or SLMs, they can be made much smaller, requiring significantly less electrodes (at least by an order of magnitude) and may be fabricated at very low cost (at least by 2–3 orders of magnitude). Such devices have been successfully used for miniature cameras with 1.5–2 mm optical clear apertures (CAs) [5,7]. Despite the fact that the maximal optical path differences $OPD = \Delta n L$ (where Δn is the optical birefringence and L is the thickness of the LC layer [8]) of such components are usually much larger compared to LCDs or SLMs, their use with devices having larger CAs still faces challenges. One possible approach here is the use of diffractive structures, but the chromatic aberrations, discrete focus, and high cost (electrodes with very small features must be etched) are important issues to consider [9–11]. Another possible approach is the use of refractive Fresnel type phase resets, and several groups, including our group, are working in this direction [12–14].

In the meantime, we have recently introduced a new design of an electrically tunable LC lens (eTLCL) allowing the generation of local lenses, the center of which may be moved over a very large CA [15]. We call them “foveal” by referring on the fact that, at each moment, only a local area of the device is usually operated. By using this eTLCL, we have successfully generated

spherical lenses with different diameters and positive (focusing) optical powers (OPs). Currently we are working on several applications of this lens. One of them is in microscopy and endoscopy (to excite and to image only the zone of interest and scan that zone dynamically [16]), while other applications are in augmented reality glasses and virtual reality headsets.

In the present work, we continue its exploration, and we show that the same design allows much richer functionalities, including the generation of an almost free-axis astigmatism, tip/tilt, etc. In addition, we demonstrate also the generation of highly localized lenses with negative (defocusing) OP with the help of so called “dual-frequency” LCs. The article is organized in the following way. We first briefly present the structure and the operation principle of the device. Then, we discuss the metrology tools used for its characterization. Obtained results on the generation and the control of the astigmatism, defocus, and tip/tilt are then presented. Finally, a preliminary experimental demonstration of a localized lens is presented for a negative OP, followed by discussions and conclusions.

2. STRUCTURE AND OPERATING PRINCIPLE

A. Lens Design and Operation Principle

The structure and the general operation principle of the proposed device were already reported in [15,17]. As a short reminder, it consists of two glass substrates coated by indium tin oxide (ITO) transparent conductive layers, which are lithographically patterned into serpentine forms (Fig. 1). The width w of ITO lanes, the gap g between them, and the sheet resistance R_s of the ITO must be optimized for specific applications,

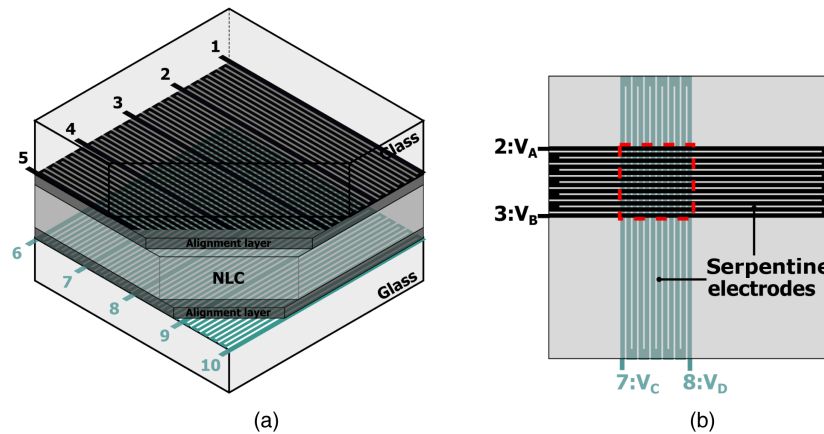


Fig. 1. (a) Schematic 3D representation of the device showing electrodes' structure, orientation, and contact electrodes' positions (e.g., 1–5 on top and 6–10 on bottom substrates), (b) top schematic view, example of a “smallest lens unit” area (shown by the dashed red rectangle), where 2–3 and 7–8 represent activated contact electrodes (on top and bottom substrates) with corresponding signals V_a , V_b , V_c , and V_d .

e.g., dynamic vision correction, panoramic or microscopic imaging, etc. There are two main criteria for this optimization: 1- to be able to generate the maximum possible modulation depth for the spatial distribution of electrical potential (from one control electrode to the other), and 2- to ensure that this spatial distribution is continuous (without discrete jumps) and not abrupt (to reduce undesired aberrations). For example, if R_o is too high, then small values of w and g will generate abrupt decrease of the electrical potential, and the resulting aberrations will be high. In contrast, if the values of w and g are too high, then there will be a discretization effect (in the distribution of the electric potential), which will generate undesired diffraction increasing the haze.

In the present implementation, we had $w = 35 \mu\text{m}$, $g = 5 \mu\text{m}$, and $R_o = 1 \text{ M}\Omega/\text{sq}$. The total working area of the device was set to $25 \text{ mm} \times 25 \text{ mm}$. The serpentine ITO pattern was connected (through periodically spaced peripheral “contact electrodes”) to an electrical driver at each 0.65 mm distance, resulting in a total of 40 electrodes on each substrate. A polyimide (PI150) alignment layer was spin-coated on each substrate, cured, and uniformly rubbed (in “antiparallel directions” [18]). Finally, these substrates were used to form a sandwich [spaced with the help of $L = 40 \mu\text{m}$ diameter beads; see Fig. 1(a)], and the space between them was filled by a commercial nematic LC (NLC) ML2608 (from Merck).

The wavefront modulation here is based on the control of the phase ϕ and the amplitude V of signals applied to control electrodes [19–21]. We can briefly present the operation principle of the device on the example of the smallest lens unit, controlled by 4 closest control electrodes V_a , V_b , V_c , and V_d , shown in Fig. 1(b). We have already demonstrated the possibility of generating tunable (with only positive OP) and scalable (with variable local CA) spherical lenses using this approach [17], when the same voltage V and an increment of 90° phase delay (ϕ) were applied to control electrodes, from V_a to V_d (that is, $\phi_a = 0^\circ$, $\phi_c = 90^\circ$, $\phi_b = 180^\circ$, and $\phi_d = 270^\circ$). Namely, when the phase delay is set to $\Delta\phi_t = \phi_a - \phi_b = 180^\circ$ on two electrodes on the same (say, top) substrate, then the root mean square (RMS) voltage profile may adopt a cylindrical shape with linear gradient (perpendicular to electrode lines) and zero

value in the center of the electrode structure. However, applying simultaneously the same phase shift of $\Delta\phi_b = \phi_c - \phi_d = 180^\circ$ on the control electrodes of the bottom substrate and maintaining a common phase shift between the top and bottom electrodes $\Delta\phi_t - \Delta\phi_b = 90^\circ$ will generate two phase shifted and spatially overlapped identical and orthogonal cylindrical shapes. The resulting rapid (for the NLC’s reaction) dynamic rotation (thanks to the 90° common phase shift) of the total electric field around the normal to cell substrates is thus generating an averaged (in time and space) conical form of electrical potential (see, e.g., [15,17]). Thus, a gradient of electric field E is formed (with E being smallest in the center and largest close to activated control electrodes, defining the “periphery” of the activated zone of interest). A corresponding dielectric torque [22,23], which is proportional to $\Delta\epsilon E^2$ (where $\Delta\epsilon$ is the dielectric anisotropy of the NLC), is then exerted on the local optical axis of the NLC (so-called “director,” representing the local average orientation of long axis of the NLC’s molecules) by E . This torque tends to reorient NLC molecules to align them with the local E , if $\Delta\epsilon$ is positive. Due to the lateral gradient of E , the corresponding reorientation angle of the director is smallest at the center ($x = 0$, where x is the radial coordinate) and largest closer to the activated control electrodes ($x = \pm r$, where r is the radius of the local lens). Respectively, a refractive index gradient $n_{\text{eff}}(x)$ is created for the extraordinary polarized wave [5]:

$$n_{\text{eff}}(x) = n_c - \frac{x^2}{2fL}, \quad (1)$$

where n_c is the effective refractive index value in the center of the lens, f is the focal distance of the generated GRIN lens, and L is the thickness of the NLC layer. This transverse modulation occurs thanks to the anisotropy of the NLC:

$$n_{\text{eff}}(\theta) = \frac{n_{\parallel}n_{\perp}}{(n_{\perp}^2 \sin^2 \theta + n_{\parallel}^2 \cos^2 \theta)^{1/2}}, \quad (2)$$

where n_{\parallel} and n_{\perp} are, respectively, extraordinary and ordinary refractive indices of the NLC ($\Delta n = n_{\parallel} - n_{\perp}$), and θ is the angle between the NLC’s director and the wavevector of the

probe light. Finally, given the parabolic form of the gradient, an OP may be generated (measured in diopters, D , or $1/m$), the maximum of which is limited by material (Δn) and geometrical parameters (r and L) of the local lens [24]:

$$OP_{\max} = 2\Delta n \cdot L/r^2. \quad (3)$$

B. Optical Metrology Tools

For a quick visual characterization of obtained wavefronts, a first (approximative) approach can be used by placing the NLC cell between two cross oriented linear polarizers with the rubbing direction (defining the ground state orientation of NLC's optical axis) being aligned at 45° with respect to the entrance polarizer's transmission axis. Then, the incident (on the NLC) light generates ordinary and extraordinary waves inside the NLC. The second polarizer (analyzer) projects both polarization components on the same axis (its transmission axis), generating thus transversally changing inferential patterns showing the relative phase shift between two polarization modes (the ordinary wave experiencing a uniform phase shift across the entire NLC); see, e.g., [8,25]. Thus, two neighboring maximums (fringes) of the obtained interference pattern represent positions where the phase shift, experienced by the extraordinary wave, is equal to 2π .

For a more quantitative approach, the wavefront of exiting, from the lens, extraordinary polarized light (at $\lambda = 633$ nm) was measured using a relay lens ($F = 50$ mm) that was projecting the exit plane of the NLC on a Shack-Hartmann (S-H) wavefront sensor (WFS30-5C(M), Thorlabs) with an optimized magnification. The plane wavefront reference was recorded when the lens was in the "off" state ($OP = 0$). The wavefront error was then determined by acquiring first 11 Zernike polynomials, and a least square Zernike fit was done to determine the weight of each aberration. We have already demonstrated in our previous work [15] that we can generate spherical positive lenses with different diameters, ranging from 1.3 to 4.55 mm, respectively, with OP values of 40 D and 3.5 D, while maintaining rather good RMS aberrations (below $\lambda/3$). It is worth mentioning that the acceptable level of aberrations depends upon the specific application, for example, some mobile imaging devices can accept total RMS values of 0.2 μm , while others, e.g., ophthalmic systems, may require significantly smaller values (below 0.1 μm).

C. Square Aperture

In most application cases, a circular aperture is used for lenses. However, the specific geometry of electrodes we are using in the foveal lens imposes a square shaped working (excitation) zone. In this section, we shall describe the corresponding particularities of obtained dynamic wave fronts, and we shall then orthogonalize (project) the Zernike polynomials (usually applied for circular apertures) on our square shaped pupil. Indeed, for a fixed position of the lens center, we can always design the final imaging device to use mostly the central circular part of it (e.g., by using a corresponding diaphragm). However, for the foveal approach, it might be useful to clarify the description method we are going to use. Usually we characterize the

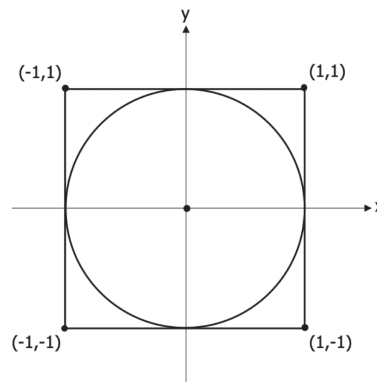


Fig. 2. Coordinate for a square pupil inscribed outside a unit circle.

wavefront \hat{W} , generated by our lens, with the help of Zernike circle polynomials Z_j , described in polar (ρ, θ) or Cartesian (x, y) coordinates as a set of orthonormal functions, while the pupil remains circular [26]. \hat{W} is expressed into Z_j with the Zernike coefficients a_j as weights, assuming that the number of base polynomials has a finite value J :

$$\hat{W}(x, y) = \sum_{j=1}^J a_j \cdot Z_j(x, y). \quad (4)$$

However, Zernike polynomials are not the best for fitting non-circular pupils and lose orthogonality over such areas. Hence, the Zernike polynomials are not appropriate for wavefront analysis of noncircular pupils. Since other polynomials can be used for the decomposition of the wavefront across a square aperture, such as 2D Chebyshev polynomials or 2D Legendre polynomials [27], circular Zernike polynomials could be orthogonalized [28,29] over a square aperture [30,31]. For square polynomials $S_j(x, y)$ being generated in Cartesian coordinates, the aberration function W for the square pupil may be expanded in terms of square polynomials that are orthonormal over the pupil weighted by square coefficients b_j :

$$W(x, y) = \sum_{j=1}^J b_j \cdot S_j(x, y). \quad (5)$$

In our case, the square aperture has regions that fall outside the unit circle (Fig. 2), which is measured by our S-H sensor; the side length of the square is a length of 2, and its area (A) is 4. The square aperture is inscribed outside of a unit circle. From S-H measurement of the circular pupil, we have orthogonalized Zernike polynomials over a square aperture. These polynomials can be obtained by using the Gram-Schmidt orthogonalization process, based on the circle Zernike polynomials, $Z_j(x, y)$, already described in detail by Mahajan [28].

3. RESULTS AND DISCUSSION

Previously, we have demonstrated that, to generate a centrosymmetric positive lens, the phase shift between signals, applied to peripheral electrodes of top and bottom substrates, must be maintained to 90° and they must have the same RMS amplitude V [15]. Based on the same principle of LCD pixels, the excitation (molecular reorientation) state is determined only by the

RMS value of the voltage difference across its row and column electrodes, regardless of the frequency of the applied signals. From Eq. (6), we can obtain the resulting RMS amplitude of the voltage between the top and bottom electrodes as equal to $\sqrt{2}V$.

In the current work, we have discovered additional control modes when we have changed independently the 4 voltage values and phase delays. In this control regime, the resulting voltage between the top and bottom electrodes is the sum of two sin waves (of same frequency) with amplitudes (V' and V'') and phase shifts (α and β) as [32]

$$\begin{aligned} V_{\text{sum}} &= V' \cdot \sin(\omega t + \alpha) + V'' \cdot \sin(\omega t + \beta) \\ &= \sqrt{[V' \cdot \cos(\alpha) + V'' \cdot \cos(\beta)]^2 + [V' \cdot \sin(\alpha) + V'' \cdot \sin(\beta)]^2} \\ &\cdot \sin \left\{ \omega t + \tan^{-1} \left(\frac{V' \cdot \sin(\alpha) + V'' \cdot \sin(\beta)}{V' \cdot \cos(\alpha) + V'' \cdot \cos(\beta)} \right) \right\}. \end{aligned} \quad (6)$$

By changing independently the voltage and phase differences between crossing electrodes, it was possible to additionally modulate the wavefront's shape (see hereafter).

A. Tunable Astigmatism

In this part of our work, we have tried to control the primary astigmatic aberration (further noted as AST). We have investigated the AST horizontal/vertical at $0^\circ/90^\circ$ (AST0/90), Fig. 3, and the AST oblique at 45° (AST45), Fig. 4. In the following section, we first discuss the influence of applied voltages on the Zernike coefficient for AST0/90. Namely, we have started by applying a voltage difference ΔV between top and bottom substrates (with $\Delta V = V_{\text{top}} - V_{\text{bot}}$, where $V_A = V_B = V_{\text{top}}$ on the top substrate and $V_C = V_D = V_{\text{bot}}$ on the bottom substrate). Figure 3(b) shows the experimentally obtained interference images confirming the desired distortion of the obtained wavefront along the horizontal and vertical axes, corresponding to x and y axes. Deforming the lens along its x-axis, where the bottom electrodes' amplitude (V_{RMS}) is higher than the amplitude applied to the top substrate, corresponds to $\Delta V < 0$ V and results in an increase of the Zernike coefficient a_6 [see Fig. 5(a)]. In contrast, distorting the lens parallel to its y-axis, where the bottom electrodes' amplitude is lower than the top one (corresponds to $\Delta V > 0$ V), causes the same coefficient to decrease. The absolute values of this change in a_6 coefficient are approximately the same. The a_6 coefficient evolves linearly with the applied voltage difference, its sign depending on the axis, related to the sign of ΔV , if $V_{\text{top}} > V_{\text{bot}}$, $a_6 < 0$ μm . Otherwise, if $V_{\text{top}} < V_{\text{bot}}$, then $a_6 > 0$ μm .

Furthermore, we have also demonstrated [in Fig. 4(b)] that the adjustment of the phase delay (see Table 1) between 4 signals deforms the lens along the oblique axis (AST45) and induces an increase/decrease of the corresponding Zernike coefficient a_5 [cf. Fig. 5(b)], with positive and negative signs depending on axis orientation $+45^\circ$ or -45° , respectively. Here, we can see also the proportionality between the phase difference on top/bottom substrates and the corresponding coefficient values.

Indeed, in this work, we have decided to change the relative phase shift compared to the standard spherical lens approach, where signals, applied to top and bottom electrodes, are always

Table 1. Amplitude and Phase Settings between Orthogonal Electrodes Used to Generate Astigmatism along the Desired Axis

Fig.	a	b	c	d	e	f	g	h	i	j
Axis ($^\circ$)	0	25	35	49	61	90	112	123	150	155
$\Delta\varphi$	0	+10	+15	+15	+10	0	-10	-15	-15	-10
ΔV	-1	-0,8	-0,4	0	+0,4	+1	+1	0,2	-0,6	-0,8

phase shifted by 90° . As an example, we show the case where the phase delay between substrates is set to 60° phase shift. Signals of the top substrate were maintained at the initial configuration $\varphi_a = 0^\circ$ and $\varphi_b = 180^\circ$, while the phases of signals, applied to the bottom substrate, were changed to $\varphi_c = 60^\circ$ and $\varphi_d = 240^\circ$. Correspondingly, based on Eq. (6), the voltage along the four corners of the lens changed; it became $V_{c/a} = V_{d/b} = \sqrt{3}V$ and $V_{c/b} = V_{d/a} = V$. This allowed us to control the AST45. To simplify the configuration notation, we considered $\Delta\varphi$ as phase variation from the initial phase delay between top/bottom electrodes, $\Delta\varphi = \varphi_c - 90^\circ$, in this example, $\Delta\varphi = -30^\circ$. It is important to notice that here we have maintained the phase

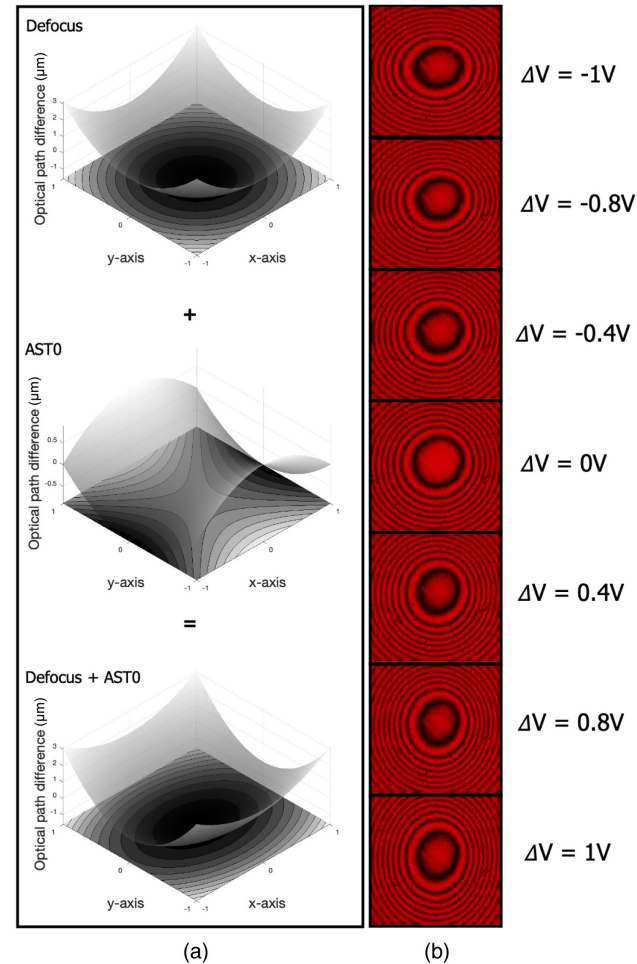


Fig. 3. (a) Digitally reconstructed wavefronts by using square Zernike polynomials (described in the main text), coupling AST0, and defocus from $a_6 = 0.375$ μm and $a_4 = 1.7$ μm , respectively; (b) experimentally obtained polarimetric images, confirming the generation of tunable vertical/horizontal astigmatism (AST0) with amplitude difference ΔV applied between top and bottom electrodes.

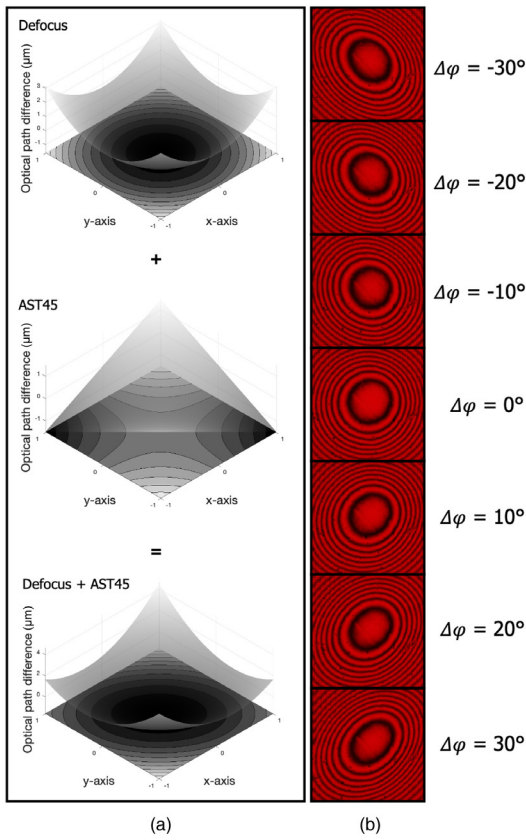


Fig. 4. (a) Digitally reconstructed wavefronts with a square aperture, coupling AST45, and defocus with $a_5 = 0.5 \mu\text{m}$ and $a_4 = 1.7 \mu\text{m}$, respectively; (b) experimental generation of tunable oblique astigmatism (AST45) with phase shift control $\Delta\varphi$.

shift between two parallel electrodes at 180° during all the experiments.

The astigmatism tunability was demonstrated by keeping the defocus and other RMS aberrations almost constant (see Fig. 5). In this case, the voltage and phase differences have to be symmetric from the initial diopter settings (for demonstration here we have normalized the initial OP to 1D). Figure 6 and Table 1 summarize our demonstration that the AST45 and AST0/90 can be tuned independently. The independent control parameters are the amplitude of the electric potential for AST0/90 and the phase delay of the signals for AST45 (thanks to the difference between top and bottom electrodes in both cases).

The summary of results obtained in different driving modes is presented in Fig. 5. Thus, we can see how to evolve Zernike coefficients ($\text{AST45} = a_5$ and $\text{AST0} = a_6$) and the corresponding OP and RMS aberrations for various amplitude [Fig. 5(a)] and phase [Fig. 5(b)] settings. The details of these settings are, respectively, shown in Figs. 5(c) and 5(d).

Further, we have measured Zernike coefficients a_5 and a_6 of AST0/90 and AST45, respectively. The S-H has been measured over an inner circular pupil of the square aperture lens, and we have converted those coefficients into square coefficients b_5 and b_6 . During all these experiments, we have maintained the diopter constant and increased or decreased the astigmatism coefficients. Moreover, without considering primary astigmatism, the aberration wavefront error RMS still remained fixed. The combination of both approaches allowed us to generate free-axis astigmatism. In this control regime, we have simultaneously generated AST0/90 combined with AST45, an independent control on $a_5 + a_6$ values inducing a free rotation of AST (see arbitrary axis generation in Fig. 6).

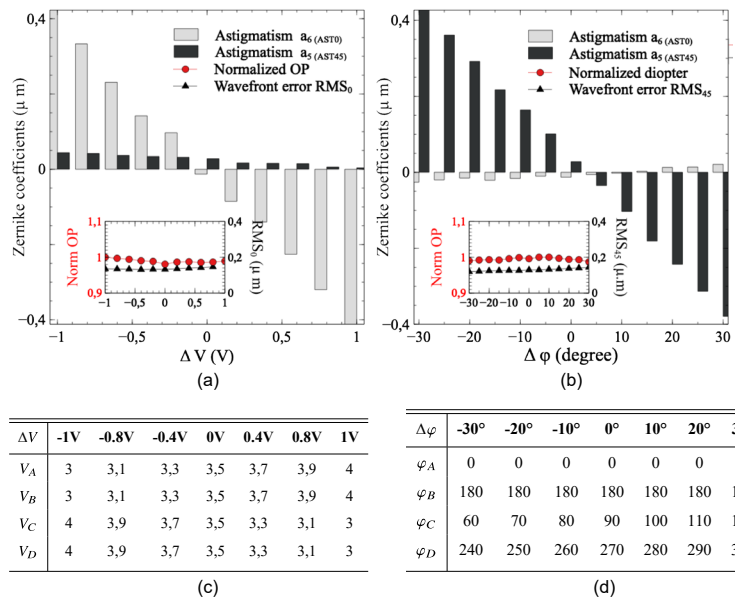


Fig. 5. Different driving modes and corresponding astigmatism Zernike coefficients ($\text{AST45} = a_5$ and $\text{AST0} = a_6$); (a) and (b) each bar shows the dependence of the Zernike coefficient's variation on the applied electric field. Optical power (OP) variation is represented by red circles, and the total RMS aberrations (without considering astigmatism and defocus) are plotted by black triangles; (c) and (d) amplitudes and phase settings on electrodes A, B, C, and D for AST45 and AST0 generation, respectively.

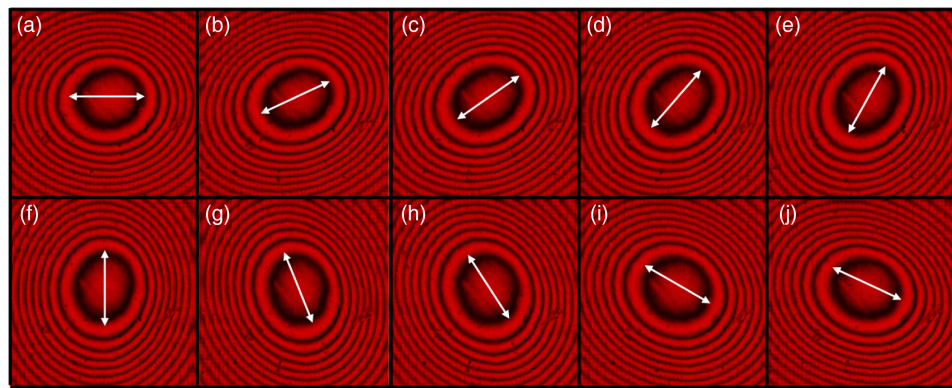


Fig. 6. Examples of generating astigmatism with precise control along arbitrary (desired) directions.

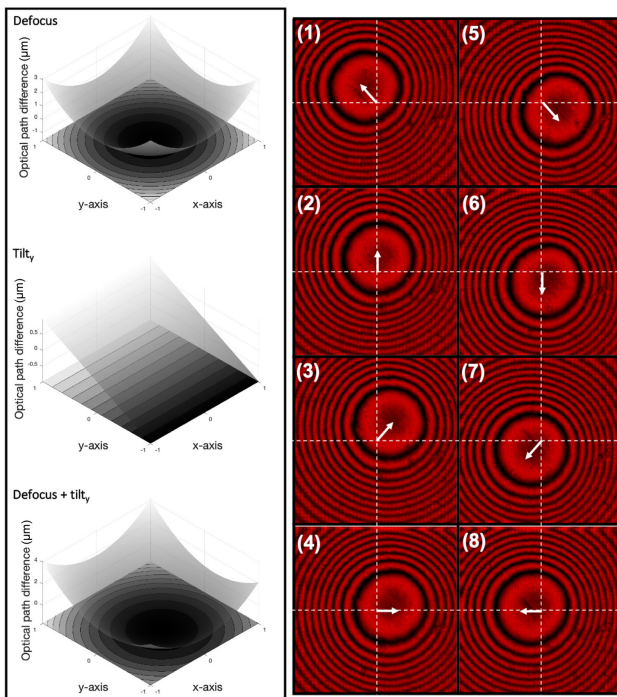


Fig. 7. (a) Digital wavefront reconstruction of $Tilt_y$, $b_2 = 0.8 \mu\text{m}$ and defocusing $b_4 = 1.7 \mu\text{m}$ aberrations; (b) experimental demonstration of tilt and defocus control. These configurations are chosen for demonstration purpose with $\Delta V = 0.8 \text{ V}$, showing several combinations of $Tilt_x + Tilt_y + \text{Defocus}$.

B. Tunable Tilt

We have then proceeded to the demonstration of simultaneous control of tilt and defocus modulation. These configurations are chosen for demonstration purposes with $\Delta V_T = 0.8 \text{ V}$, showing several combinations of $Tilt_x$, $Tilt_y$ combined to defocus. We have measured the corresponding Zernike coefficients a_2 , a_3 , and a_4 under different tilt conditions (see Fig. 7).

The distortion is a tilt, depending on the field. The idea behind the proposed system is to use an active optical element to adjust in real time the distortion of the system. Distortion is not an aberration that affects the image quality by changing the spot size, but an aberration that changes the local lens magnification.

Table 2. Amplitude Setting on Electrodes A, B, C, and D for Defocus + Tilt Generation

Fig.	1	2	3	4	5	6	7	8
V_A	3.2	3.5	3.8	3.8	3.8	3.5	3.2	3.2
V_B	3.8	3.5	3.2	3.2	3.2	3.5	3.8	3.8
V_C	3.2	3.2	3.2	3.5	3.8	3.8	3.8	3.5
V_D	3.8	3.8	3.8	3.5	3.2	3.2	3.2	3.5

As we can see, the center of the concentric interference fringes changes with the relative lateral shift (see also similar tuning in [33,34]). The corresponding excitation voltages are shown in Table 2.

C. Negative Lens

The above description illustrates how we can generate various positive lens profiles. While these are rather advanced wavefronts, the proposed design allows the generation of much richer wavefronts. This includes also bipolar responses (with both positive and negative OP values) [14,35,36]. Such a bipolar response may add significant capabilities in future applications (including the compensation of myopia, along with all other types of possible aberrations of human vision).

While we realize that it will require a separate more detailed study of this bipolar capability of our lens, we think that it might be useful to make the demonstration of its feasibility here. For this demonstration, we have used a so-called dual frequency NLC (DFNLC). As it was already described [37,38], a DFNLC exhibits a frequency dependent inversion of the sign of its dielectric anisotropy $\Delta\epsilon$. Thus, an electric field with a high frequency F that is above the inversion (so-called *crossover*) frequency f_c forces the NLC director to realign in the perpendicular (to the field) plane since $\Delta\epsilon$ is negative. In the meantime, a field with low frequency f (below the f_c) is orienting molecules along the field [39] since the $\Delta\epsilon$ is positive. If both high and low frequency fields are applied almost simultaneously, then the NLC responds essentially to the difference of the opposing torques and settles at a corresponding equilibrium.

In our demonstration, the low frequency electric field propagates well in the transverse plane and forces molecules to align (almost uniformly) perpendicular to the substrates of the cell. Then a high frequency field, controlled by using standard phase shifts, as described earlier [15,17], partially reorients molecules

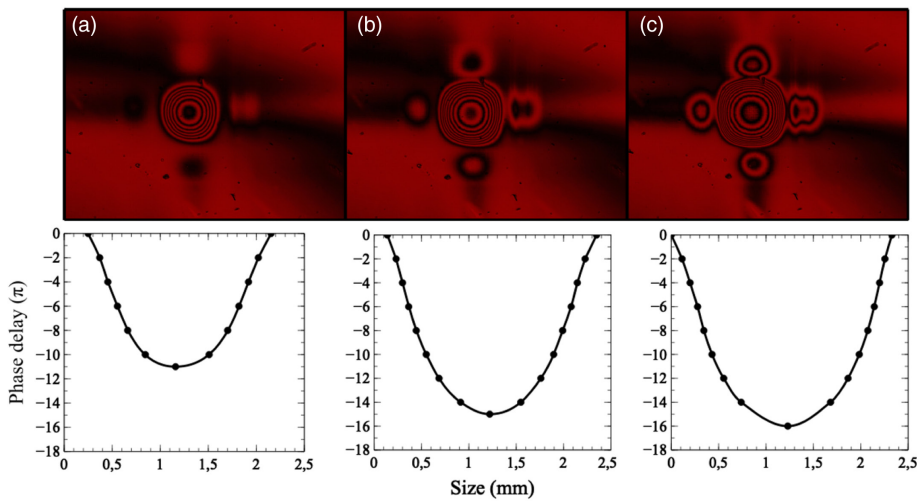


Fig. 8. Demonstration of the possibility of generating and controlling a tunable negative lens with CA = 2.3 mm [(a)–(c): top pictures show the polarimetric images, obtained for different optical power values, while the bottom curves show the corresponding reconstructed waveforms] (obtained from polarimetric data).

back to the parallel state in areas of the cell that are closest to the peripheral (activated) electrodes. Thus, we can start from a planar aligned cell (in the ground-state) and obtain lenses with negative OP. In addition, by keeping external (beyond the peripheral) electrodes on the ground state, we can obtain a highly localized negative lens, which may be tuned, scaled, and moved through the entire area.

In the example of Fig. 8, a local lens of CA = 2.3 mm is shown. The high frequency drive signal was fixed at F = 30 kHz, and its amplitude was VF = 6 V_{RMS}, while the low frequency was f = 20 Hz, and we have only adjusted its amplitude Vf to change the OP of the lens. The 3 examples here are obtained for the values of Vf equal to 3.2 V_{RMS}, 3.5 V_{RMS}, and 3.8 V_{RMS} for Figs. 8(a), 8(b), and 8(c), respectively. External (beyond peripheral) electrodes are in the ground state.

Here, our preliminary results show that the ITO serpentine resistivity must be further optimized to help the electric potential with high frequency to propagate further towards the center of the local lens (from peripheral electrodes). With this method, we are able to scale and to generate a negative tunable lens with free axis astigmatism too.

4. SUMMARY AND CONCLUSION

We have used the same design as in our previous work [15], but we have used different control approaches that allowed us the generation of advanced wavefront control capabilities. Indeed, a rather high level of independent control of aberrations was achieved by a relatively simple technique: applying different voltages and phase delays to 4 control electrodes (defined by the zone of interest). For example, among others, we have proposed a method to generate an astigmatism with almost arbitrary axis and arbitrary values, and we have experimentally demonstrated the possibility of controlling the magnitude and the orientation of the AST vector axis. Moreover, the tuning focus range could be extended by increasing or decreasing electrical amplitude signals on four peripheral electrodes.

The presence of astigmatism in an optical system implies that rays of the sagittal plane and rays of the meridional plane are focused at different planes perpendicular to the optical axis. This results in a directional blurring of the obtained image. Thus, the accurate control of astigmatism value and orientation (reported here) will allow the control of wavefront aberrations of many optical systems, especially for vision (eye) correction. If we consider an eyeglass prescription, it consists of spherical power D_r , cylindrical power C_r (related to astigmatism value), and an axis direction θ_r diagnostic. An estimation of the direction of astigmatism axis (θ_r in degrees) and its OP from the measured Zernike coefficients may be easily obtained [40].

We have also demonstrated a variable tilt by applying a simple electrical modulation technique. All these demonstrations were done on arbitrary positions over the entire clear aperture.

We think that the above-mentioned capabilities might be also very useful for augmented and virtual reality headsets, among others, to address the ophthalmic eye-glass or vergence-accommodation [41] problems, which are the subject of active research efforts today [42].

Despite the noncircular pupil of the device, we have used a method of transforming the Zernike coefficients for quantitative wavefront analysis over square shaped apertures. In this case, outer square coefficients can be derived from Zernike coefficients.

Furthermore, we have also demonstrated (in a very preliminary way) the possibility of generation of highly localized (throughout the entire surface of the device) negative lenses by using DFNLC. It will also allow us to obtain faster responses, if needed by the specific application.

We think that this device has rather unique features to be discovered yet. Its spectral, dynamic, and other technical characteristics (e.g., haze) are very similar to traditional single “fixed” aperture lenses (see, e.g., [5]). In addition, its manufacturing is simple (single lithography step is required) and can be done in a very cost-effective way.

There is no doubt that it will enable a significant enhancement of adaptive capabilities of various optical systems and will find multiple applications in imaging and/or vision. The specific choices of parameters of the lens (electrodes' width and spacing, sheet resistance of the ITO, type of the NLC, etc.) must be done in the framework of a specific target application to optimize its performances.

Funding. Natural Sciences and Engineering Research Council of Canada (NSERC) (05888); Canada Research Chairs (CRC) (230212).

Acknowledgment. We would like to acknowledge LensVector Inc., the NSERC, and the CRC in Liquid Crystals and Behavioral Biophotonics for their financial support of this work.

Disclosures. The authors have no conflict of interest to disclose.

Data availability. Detailed data underlying the results presented in this paper are not publicly available at this time but may be obtained from authors upon request.

REFERENCES

1. S. S. Reza, "A review paper on liquid crystal display," *Int. J. Opt. Sci.* **5**, 5–8 (2019).
2. J. Huignard, "Spatial light modulators and their applications," *J. Opt.* **18**, 181 (1987).
3. S. Sato, "Applications of liquid crystals to variable-focusing lenses," *Opt. Rev.* **6**, 471–485 (1999).
4. A. Naumov, M. Y. Loktev, I. Guralnik, et al., "Liquid-crystal adaptive lenses with modal control," *Opt. Lett.* **23**, 992–994 (1998).
5. T. Galstian, O. Sova, K. Asatryan, et al., "Optical camera with liquid crystal autofocus lens," *Opt. Express* **25**, 29945–29964 (2017).
6. Y.-H. Lin, Y.-J. Wang, and V. Reshetnyak, "Liquid crystal lenses with tunable focal length," *Liq. Cryst. Rev.* **5**, 111–143 (2017).
7. T. Galstian, *Smart Mini-cameras* (CRC Press, 2014), Vol. **258**.
8. L. Begel and T. Galstian, "Liquid crystal lens with corrected wavefront asymmetry," *Appl. Opt.* **57**, 5072–5078 (2018).
9. P. Valley, D. L. Mathine, M. R. Dodge, et al., "Tunable-focus flat liquid-crystal diffractive lens," *Opt. Lett.* **35**, 336–338 (2010).
10. Z. Luo, Y. Li, J. Semmen, et al., "Achromatic diffractive liquid-crystal optics for virtual reality displays," *Light Sci. Appl.* **12**, 230 (2023).
11. E. Otón, P. Morawski, R. Mazur, et al., "Diffractive and refractive liquid crystal devices based on multilayer matrices," *J. Lightwave Technol.* **37**, 2086–2093 (2019).
12. A. Jamali, D. Bryant, A. K. Bhowmick, et al., "Large area liquid crystal lenses for correction of presbyopia," *Opt. Express* **28**, 33982–33993 (2020).
13. O. Sova and T. Galstian, "Modal control refractive Fresnel lens with uniform liquid crystal layer," *Opt. Commun.* **474**, 126056 (2020).
14. O. Sova, V. Presniakov, A. Zohrabyan, et al., "Large diameter electrically tunable lens for ophthalmic distance accommodation," *Biomed. Opt. Express* **14**, 6317–6327 (2023).
15. L. Bégel, B. Khodadad, and T. Galstian, "Adaptive lens for foveal vision, imaging, and projection over large clear apertures," *Opt. Express* **31**, 2877–2891 (2023).
16. L. Tabourin, F. Bretzner, and T. Galstian, "Towards a mini-endoscope design with spatially selective excitation and imaging," *Biomed. Opt. Express* **15**, 1750–1760 (2024).
17. J. Stevens and T. Galstian, "Electrically tunable liquid crystal lens with a serpentine electrode design," *Opt. Lett.* **47**, 910–912 (2022).
18. K. Takatoh, M. Sakamoto, R. Hasegawa, et al., *Alignment Technology and Applications of Liquid Crystal Devices* (CRC Press, 2005).
19. S. P. Kotova, V. V. Patlan, S. Samagin, et al., "Tunable liquid-crystal focusing device. 1. Theory," *Quantum Electron.* **41**, 58 (2011).
20. S. P. Kotova, V. Patlan, and S. A. Samagin, "Tunable liquid-crystal focusing device. 2. Experiment," *Quantum Electron.* **41**, 65 (2011).
21. S. Kotova, A. Mayorova, D. Prokopova, et al., "Tunable liquid crystal astigmatic plate," *J. Phys. Conf. Ser.* **1368**, 022018 (2019).
22. P.-G. De Gennes and J. Prost, *The Physics of Liquid Crystals* (Oxford University, 1993), Vol. **83**.
23. L. M. Blinov and V. G. Chigrinov, *Electrooptic Effects in Liquid Crystal Materials* (Springer, 1996).
24. L. Begel and T. Galstian, "Dynamic compensation of gradient index rod lens aberrations by using liquid crystals," *Appl. Opt.* **57**, 7618–7621 (2018).
25. L. Tabourin and T. Galstian, "Liquid crystal module for motionless generation of variable structured illumination," *J. Opt. Soc. Am. B* **37**, 2064–2070 (2020).
26. V. Lakshminarayanan and A. Fleck, "Zernike polynomials: a guide," *J. Mod. Opt.* **58**, 545–561 (2011).
27. J. Ye, Z. Gao, S. Wang, et al., "Comparative assessment of orthogonal polynomials for wavefront reconstruction over the square aperture," *J. Opt. Soc. Am. A* **31**, 2304–2311 (2014).
28. V. N. Mahajan and G.-M. Dai, "Orthonormal polynomials for hexagonal pupils," *Opt. Lett.* **31**, 2462–2464 (2006).
29. V. N. Mahajan, "Orthonormal polynomials in wavefront analysis," in *Proceedings of the Optical Society of Korea Conference* (Optical Society of Korea, 2009), pp. 50–51.
30. A. H. Al-Hamdan and S. Y. Hasan, "Zernike polynomials for optical systems with rectangular and square apertures of area equal to," *NIScPR* (2013).
31. G.-M. Dai and V. N. Mahajan, "Orthonormal polynomials in wavefront analysis: error analysis," *Appl. Opt.* **47**, 3433–3445 (2008).
32. R. Lyons, "Sum of two sinusoids," For free publication by IOWEGIAN (2011).
33. W. Feng, Z. Liu, and M. Ye, "Liquid crystal lens with a shiftable optical axis," *Opt. Express* **31**, 15523–15536 (2023).
34. M. Ye, B. Wang, and S. Sato, "Liquid crystal lens with focus movable in focal plane," *Opt. Commun.* **259**, 710–722 (2006).
35. B. Wang, M. Ye, and S. Sato, "Liquid crystal lens with focal length variable from negative to positive values," *IEEE Photonics Technol. Lett.* **18**, 79–81 (2005).
36. Z. Zemska and T. Galstian, "Electrically tunable lens with a non-monotonic wavefront control capability," *Opt. Lett.* **47**, 4287–4290 (2022).
37. A. K. Kirby, P. J. Hands, and G. D. Love, "Liquid crystal multi-mode lenses and axicons based on electronic phase shift control," *Opt. Express* **15**, 13496–13501 (2007).
38. O. Pishnyak, S. Sato, and O. D. Lavrentovich, "Electrically tunable lens based on a dual-frequency nematic liquid crystal," *Appl. Opt.* **45**, 4576–4582 (2006).
39. O. A. Zayakin, M. Y. Loktev, G. D. Love, et al., "Cylindrical adaptive lenses," *Proc. SPIE* **3983**, 112–117 (1999).
40. R. Kosaki, N. Maeda, K. Bessho, et al., "Magnitude and orientation of Zernike terms in patients with keratoconus," *Invest. Ophthalmol. Visual Sci.* **48**, 3062–3068 (2007).
41. G. Kramida, "Resolving the vergence-accommodation conflict in head-mounted displays," *IEEE Trans. Visual Comput. Graph.* **22**, 1912–1931 (2015).
42. S. Charrière and L. Duveau, "A vergence accommodation conflict-free virtual reality wearable headset," *Proc. SPIE* **10676**, 242–256 (2018).